INSTITUTE OF PHYSICS PUBLISHING JOURNAL OF PHYSICS: CONDENSED MATTER

J. Phys.: Condens. Matter **18** (2006) S933–S947 doi:10.1088/0953-8984/18/25/S02

Deformation textures produced in diamond anvil experiments, analysed in radial diffraction geometry

H-R Wenk, I Lonardelli, S Merkel, L Miyagi, J Pehl, S Speziale and C E Tommaseo

Department of Earth and Planetary Science, University of California, Berkeley, CA 94720, USA

Received 17 November 2005, in final form 14 March 2006
Published 8 June 2006
Online at stacks.iop.org/JPhysCM/18/S933

Abstract

Diamond anvil cells may not only impose pressure upon a sample but also a compressive stress that produces elastic and plastic deformation of polycrystalline samples. The plastic deformation may result in texture development if the material deforms by slip or mechanical twinning, or if grains have a non-equiaxed shape. In radial diffraction geometry, texture is revealed by variation of intensity along Debye rings relative to the compression direction. Diffraction images (obtained by CCD or image plate) can be used to extract quantitative texture information. Currently the most elegant and powerful method is a modified Rietveld technique as implemented in the software package MAUD. From texture data one can evaluate the homogeneity of strain in a diamond anvil cell, the strain magnitude and deformation mechanisms, the latter by comparing observed texture patterns with results from polycrystal plasticity simulations. Some examples such as olivine, magnesiowuestite, $MgSiO_3$ perovskite and ε-iron are discussed.

1. Introduction

The deep earth is not accessible to direct observation and most information about its structure and composition relies on interpretation of geophysical data, mainly seismic evidence. Much information on potential phase relations has been gained from experiments at high pressure and high temperature. Of those, shock compression and diamond anvil cells have been essential [1]. In many sectors of the earth there is evidence for dynamic processes that produce heterogeneity and anisotropy. Thus mechanical properties of minerals, influencing the plastic and elastic behaviour as well as the rheology, have become of great interest to the geophysics community. Currently it is not possible to perform quantitative deformation experiments in large volume apparatus to constrain flow laws beyond pressure conditions of the transition zone [2, 3] and models based on first principles still poorly constrain the deformation behaviour [4–6], leaving much uncertainty about deformation mechanisms at ultrahigh pressure. Of considerable interest has been observation of seismic anisotropy in the earth that can be interpreted as evidence for

deformation, producing preferred orientation. In order to understand seismic anisotropy one needs to know the elastic tensor of crystals and microscopic mechanisms that align them during deformation. Both can be addressed with diamond anvil cells (DAC), but using a radial, rather than the conventional axial, diffraction geometry.

In addition to confining pressure, an axial compressive stress is imposed by the diamonds, as has been established by finite element modelling [7], and in a radial diffraction geometry Debye rings reveal variations in d-spacings and intensity of lattice planes that are in different orientations relative to the compression direction. The radial diffraction geometry in DAC experiments was introduced by Kinsland and Bassett [8] and used by Hemley *et al* [9] to investigate stresses and elastic properties up to megabar pressures [10]. Intensity variations along Debye rings are indicative of preferred orientation (texture) that is evidence for crystal rotations due to plastic deformation. In this paper we will review some aspects of the radial diffraction technique to obtain texture information at high pressure and illustrate it with examples. It has been observed that many materials, brittle at ambient conditions, become ductile at pressure above 5 GPa, even at room temperature (olivine, periclase, perovskite and spinel are examples). We will focus on *in situ* texture measurements and discuss how texture patterns can be interpreted to indicate intracrystalline deformation mechanisms as well as overall strain.

Right up front it should be made clear that the DAC deformation experiments are by no means ideal to investigate the rheology of earth materials, which depends on many factors such as stress, strain rate, pressure, temperature, grain size and composition [11, 12], including water content as in the case of quartz [13] and olivine [14–16]. Diffraction volumes in DAC experiments are small, strain as well as stress may be heterogeneous, it is not possible to separate pressure from stress, stresses are generally very large, and at most facilities it is not possible to conduct radial diffraction experiments *in situ* at high temperature. Despite these deficiencies, radial DAC remains the only method to conduct deformation experiments at pressures corresponding to the lower mantle, the D″ zone and the solid inner core and to investigate texture development of phases such as $MgSiO_3$ perovskite and postperovskite, $CaSiO_3$ perovskite and rhombohedral FeO, as well as ε-iron, that are unstable at ambient conditions and can either not be quenched or suffer substantial obliteration of microstructural details when decompressed to ambient conditions.

2. Experiments and data analysis

2.1. DAC experiments

DAC experiments use the x-ray and optical transparency of diamonds to conduct spectroscopic as well as diffraction experiments at high pressure. Depending on the application, polychromatic or monochromatic x-rays are used. For the experiments reported here we use monochromatic x-rays and diffraction patterns are recorded with a 2D detector positioned perpendicular to the incident beam. CCD detectors have the advantage of fast readout, while image plates have higher resolution and a larger dynamic range, but are slower.

In conventional geometry the beam enters along the diamond axis and the diffraction pattern contains information about lattice planes that are oriented close to parallel to the incident x-ray, thus—in axial geometry—the DAC axis. If only phase relations are of interest this is the preferred geometry because of the high transparency of diamond along the ray path. Often efforts are made to obtain hydrostatic pressure by immersing the sample in a gas or liquid. Without such precautions diamond pistons not only produce confining pressure but also a compressive stress, and the material deforms elastically as well as plastically (figure 1).

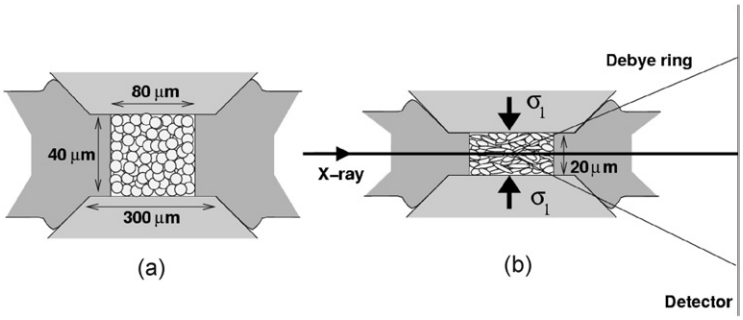

Figure 1. Schematic of a radial DAC cell that is used a deformation apparatus. (a) Initial dimensions, (b) deformed dimensions and diffraction geometry.

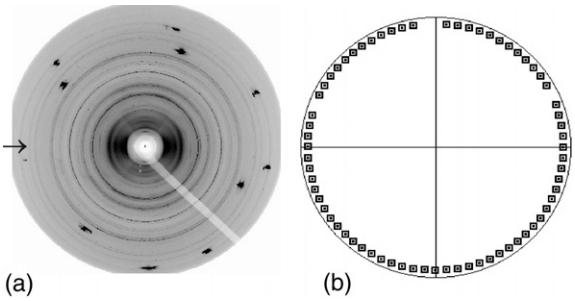

Figure 2. (a) Diffraction image of $MgSiO_3$ perovskite transformed from enstatite, collected *in situ* at 43 GPa with an image plate detector at APS-HPCAT. Strong intensity spots are due to diffractions from diamond. The compression direction is indicated with an arrow. (b) Pole figure coverage for a Debye ring.

In radial diffraction geometry, the beam passes through the DAC perpendicular to the axis (figure 1(b)) and in this case Debye rings in diffraction patterns record a whole range of orientations, with lattice planes from parallel to nearly perpendicular to the DAC axis. The diffraction pattern illustrates elastic deformation effects expressed in elliptical distortions of Debye rings and intensity variations that signify texture, as for $MgSiO_3$ perovskite at 42 GPa in figure 2(a) (the compression direction is indicated with an arrow). Both the elliptical distortion and the intensity variations are best seen if we 'cake' the diffraction pattern by 'unrolling' it, e.g. in Fit2D (figure 3). *Elastic deformation* appears as sinusoidal variations in d-spacings that are smaller (and correspondingly diffraction angles θ are larger) perpendicular to the compression direction (arrow). The changes in d-spacings depend upon the applied compressive stress and elastic properties. In the case of MgO, where elastic properties are well known, deviatoric stresses ranging from 5 to 9 GPa (above 10 GPa confining pressure) have been observed [17]. This value depends on material and gasket type. *Plastic deformation* is expressed in intensity variations that signify preferred orientation, attained e.g. through dislocation glide.

In contrast to the axial geometry, in radial geometry x-rays not only pass through diamond and sample but also through a gasket that maintains the pressure (figure 1(b)). The diffraction pattern shown in figure 2(a) not only contains diffraction from the sample but from the gasket and diamonds as well. Diamond diffractions are visible as high intensity spots. In figure 2(a), diffraction from the confining Kapton gasket produces diffuse rings at low scattering angles.

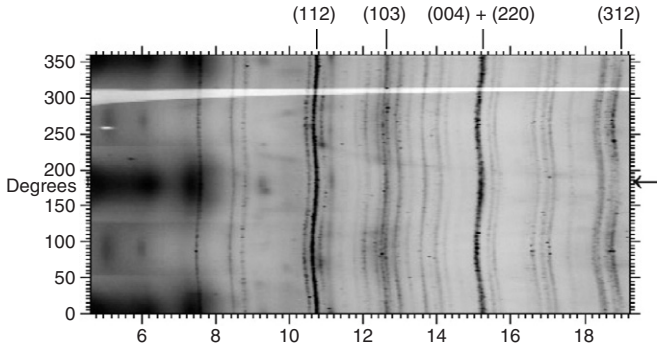

Figure 3. Unrolled diffraction image (figure 2(a)) in Fit2D, plotting azimuthal angle along the Debye ring as a function of Bragg angle θ. The sinusoidal variations in diffraction lines are due to elastic deformation; intensity differences along lines indicate preferred orientation caused by plastic deformation. Compression direction is indicated by the arrow.

Furthermore, the incident x-ray passes through the peripheral and central portions of the sample, and, if there are gradients in pressure, stress and temperature, the diffraction signal provides an average that needs to be deconvoluted. To facilitate the interpretation of diffraction images, experiments need to be designed to minimize gradients and signals from the gasket material.

Gaskets are mainly chosen for strength, combined with x-ray transparency. A favourite material has been Be, that can be used beyond 200 GPa [9]. A disadvantage is that Be scatters strongly and its diffraction lines may overlap with the much weaker lines from the sample, making the analysis difficult. Tilting the DAC 20°–30° can reduce or eliminate this interference. For moderate pressures (<50 GPa) gaskets produced by mixing a powder of amorphous boron with epoxy can be used [17, 18]. This is particularly efficient if the size of the boron gasket is minimized by enclosing a small disk in a ring of x-ray transparent Kapton [19]. No doubt more flexible designs will be developed in the future. As will be shown later, the present gasket geometry limits the strain to about 20%. Preferred orientation generally develops quickly and stabilizes, changing little upon further compression.

2.2. Image analysis

The image in figure 3 illustrates some complications often encountered in the radial diffraction data analysis. There are many diffraction lines; some of these are partially or completely overlapped. Also, background intensities vary as a function of azimuthal angle, mainly due to differences in absorption. An efficient and quantitative approach to analyse such images is the Rietveld method, that applies a physical model to express spectral intensities and refines instrumental parameters (e.g. image position, resolution, background), sample characteristics (absorption, microstructure), crystallographic properties (e.g. lattice parameters and atomic coordinates) and stress (using an appropriate model), as well as texture, our primary interest. We apply the Rietveld method in the MAUD software, that is unique in implementing advanced direct methods of quantitative texture analysis [20, 21].

Images must be calibrated with a standard for wavelength and sample–detector distance. After being centred, the image is decomposed into spectra by integrating over azimuthal sectors (usually 5°, 10° or 15°). As an example, two of these spectra with experimental data and the Rietveld fit are shown in figure 4(a). Indicated below the spectra are the positions of

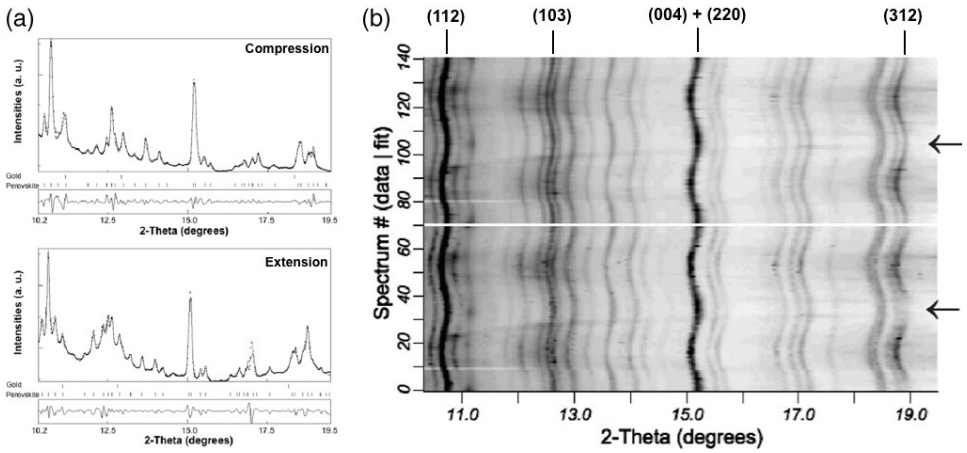

Figure 4. Rietveld method applied to diffraction image of perovskite (figure 2(a)). (a) Two experimental and fitted spectra parallel (top) and perpendicular to compression direction (bottom). (b) Map plot of stacked normalized spectra, experimental at bottom and calculated at top. Compression direction indicated by arrow.

diffraction lines and the deviations between experiment and fit. The two spectra correspond to different slices and represent different orientations relative to the compression direction. In the spectrum on top the lattice planes are perpendicular to the compression direction and in the bottom spectrum they are parallel. An overall assessment of the quality of the Rietveld fit is displayed in a 'map plot' (figure 4(b)) that compares a stack of experimental spectra (bottom) with recalculated spectra (top), expressed as grey shades. Note that not only peak intensities, but also background variations, are well reproduced.

The pole figure coverage of a Debye ring from a diffraction image with 5° integration is shown in figure 2(b). The pole figure is in the same orientation as the image (figure 2(a)) and the coverage is a ring near the periphery. Clearly this coverage is very sparse, extending roughly from parallel to perpendicular to the compression direction and, if axial symmetry (around the compression axis) is assumed, contains all information required to reconstruct a quantitative model of the orientation distribution (OD).

Often it is useful to establish if axial symmetry is indeed satisfied in an experiment and that sample rotations in the Rietveld program have been done correctly. It has been shown that a single 2D image (figure 2(a)) with a sparse coverage (figure 2(b)) can be sufficient to derive an approximate 3D OD [22]. From the OD, pole figures can be generated. In the case of the image in figure 2(a), and without imposing any sample symmetry, we obtain a (100) pole figure for perovskite with (100) lattice planes parallel to the compression direction and a (001) pole figure with (001) lattice planes perpendicular to the compression direction (figure 5(a)). Note that the sample has been rotated with respect to figure 2, to bring the compression direction into the centre. The rotated coverage is shown in figure 5(b) (compare with figure 2(b)). We verify that the pole figure symmetry is roughly axially symmetric about the diamond axis, as would be expected from the DAC geometry, and thus, in a next step of the analysis, axial symmetry can be imposed on the measured data (figure 5(c)) and the OD calculation can be refined. A compact method to represent axially symmetric textures is with inverse pole figures of the compression direction relative to crystal coordinates, as shown in figure 5(d). The (001) pole figure displays a maximum in the compression direction (figures 5(a) and (c)). This is expressed in the inverse pole figure with a maximum near (001) (figure 5(d)). In the following section we will illustrate

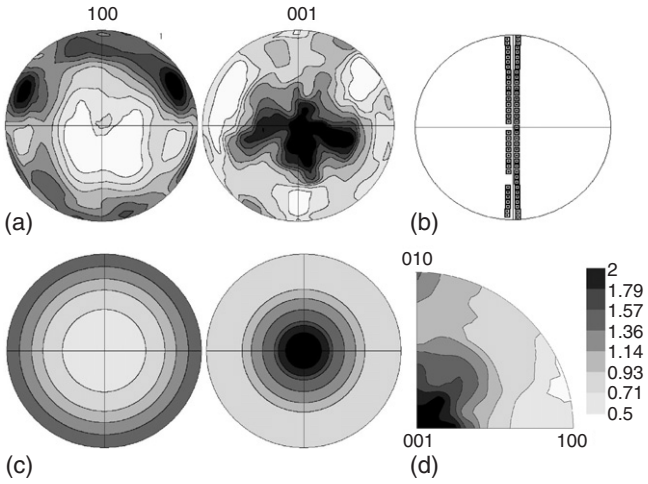

Figure 5. Texture representations of OD data obtained from the image shown in figure 2(a) for orthorhombic $MgSiO_3$ perovskite at 43 GPa. (a) (100) and (001) pole figures without imposing sample symmetry; (b) pole figure coverage; (c) (100) and (001) pole figures imposing axial sample symmetry. The compression direction is in the centre. (d) Inverse pole figure of the compression direction. Equal area projection with linear contours.

some examples of radial diffraction DAC experiments where quantitative texture information was obtained and could be interpreted.

3. Examples

The radial DAC experiments that are discussed in this report were conducted at ALS beamline 12.2.2 (wuestite, magnesiowuestite and perovskite) and APS GSECARS beamline 13-ID (olivine, perovskite, periclase and iron), APS HPCAT beamline 16-ID-B (perovskite) and BNL beamline X17-C (iron).

3.1. Olivine

The preferred orientation of olivine Mg_2SiO_4 has been of longstanding interest because of its importance for interpreting the strong seismic anisotropy in the upper mantle [23]. Numerous experimental studies documented changes in orientation patterns with temperature, strain rate, pressure and most recently water content [24, 14–16]. Olivine can be deformed in conventional deformation apparatus and DAC is not required. We use it here to test the radial DAC method to see if similar results are obtained as with other methods for corresponding conditions. Olivine powder (grain size 1–5 μm) was compressed in the DAC to 27 GPa, at which point the phase transformation to perovskite was induced by laser heating [25]. Between 10 and 15 GPa a distinct texture pattern evolved (figure 6(a)) that strengthened slightly when pressure was increased to 27 GPa (figure 6(b)). The inverse pole figures display a broad minimum at (001) and concentrations along the (100)–(110)–(010) girdle, with maximal pole densities of 1.5 multiples of a random distribution (mrd). This pattern is consistent with deformation mechanisms where [001] is the principal slip direction such as (100)[001] and {hk0}[001] pencil glide as determined for low temperature deformation of olivine [26]. Indeed, polycrystal plasticity simulations for this mechanism produce an inverse pole figure that is very similar to

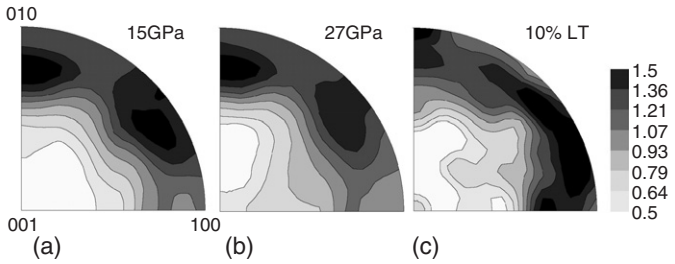

Figure 6. Inverse pole figures for olivine obtained from images measured *in situ* at (a) 15 GPa and (b) 27 GPa (APS-GSECARS). (c) Polycrystal plasticity simulation for {*hk*0}[001] pencil glide 10% strain (table 1) [25]. Equal area projection with linear contours.

Table 1. Slip systems assumed in polycrystal plasticity simulations of olivine. Critical shear stress coefficients (CRSS) and average activity at 10% strain are given (for texture pattern see figure 6(c)).

Slip system	CRSS	Activity (%)
(100)[001]	1	33
(010)[001]	1	20
(100)[010]	5	3
{110}[001]	1	44

the experimental ones (figure 6(c)). Assumed critical shear stresses on slip systems and slip system activities are summarized in table 1. The best agreement in texture strength is obtained for a shortening of 10%, which provides an estimate for the overall strain in this experiment and may be typical for many DAC experiments. This texture pattern and deformation mechanism do not apply to mantle conditions but may be significant for metamorphic rocks, and the high pressure experiments provide ductility to obtain significant plastic strains at high strain rates.

3.2. Periclase, magnesiowuestite and wuestite

Some of the early radial DAC texture experiments were done with periclase (MgO) [17]. It was observed that periclase started to deform plastically at 5 GPa confining pressure, with development of a {001} texture that became very strong upon further straining to 35 GPa, with a maximum of 9.1 mrd. This texture type indicates that only $\{110\}\langle 1\bar{1}0\rangle$ slip was significantly active. First principles calculations confirm this slip system for high pressure and low temperature [5]. At lower pressure and high temperature large volume experiments produce textures consistent with activity of {110}, {111} as well as {100} slip [27–29]. The change of slip system activity with temperature for MgO is analogous to isostructural halite where {110} slip dominates at low temperature, and {110}, {111} and {100} slip systems are equally active at higher temperature [30].

The original experiments were done with a mixture of periclase and iron [17]. More recent experiments with single phase oxides, but ranging in composition from periclase (MgO) to wuestite (FeO), confirm these results [31] but also indicate a change in texture strength with composition. Figure 7 compares inverse pole figures for 15–20 GPa confining pressure. For Mg 40% Fe 60% a strong {001} texture develops, similar to pure MgO (figure 7(a); the maximum is 7 mrd). For the same pressure but for Mg 25% Fe 75% the texture is much attenuated (figure 7(b), 2.3 mrd), and for Mg 10% Fe 90% even weaker (figure 7(c), 1.2 mrd). With increasing iron content, magnesiowuestite becomes more compressible [32, 33] and it is

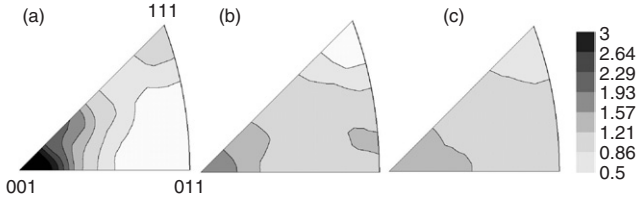

Figure 7. Inverse pole figures for magnesiowuestite. (a) $Fe_{0.60}Mg_{0.40}O$, 16 GPa (APS-HPCAT); (b) $Fe_{0.75}Mg_{0.25}O$, 16 GPa (ALS-12.2.2); (c) $Fe_{0.90}Mg_{0.10}O$, 18 GPa (ALS-12.2.2) [31]. Equal area projection, linear contours.

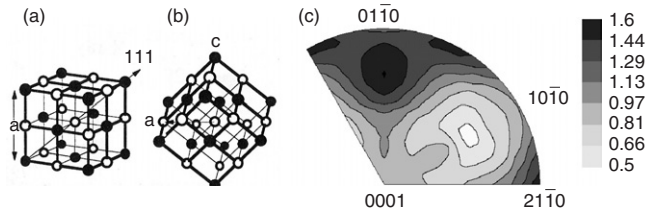

Figure 8. Transformation of cubic B1 wuestite (a) to rhombohedral wuestite (b) by a distortion of the lattice [18]. (c) Inverse pole figure of rhombohedral wuestite at 25 GPa (ALS-12.2.2). Equal area projection, linear contours.

plausible that for high Mg content, plastic deformation dominates, whereas for high Fe content elastic deformation may contribute significantly to the accommodation of the moderate strain.

Iron-rich magnesiowuestite undergoes a phase transformation from cubic to rhombohedral at high pressure (20 GPa) [18, 34–36]. The transformation corresponds to a displacive distortion of the B1 structure (figure 8(a)) along one body diagonal (figure 8(b)). Interestingly, when cubic FeO transforms to rhombohedral FeO under stress, it displays immediately a strong texture with a maximum at $\{01\bar{1}2\}$ (figure 8(c)). The $\{01\bar{1}2\}$ planes of the rhombohedral phase (hexagonal setting) correspond to {001} lattice planes in the cubic structure. It is conceivable that this texture develops by transformation twinning with variant selection due to stress.

3.3. $MgSiO_3$ perovskite

Textures of perovskites are not only relevant for geophysics, since they constitute the major phase in the lower mantle [37], they are also of interest to materials science as important ferroelectrics [38]. Perovskite occurs in cubic, tetragonal and orthorhombic structures [39]. Orthorhombic $MgSiO_3$ perovskite (space group *Pbnm*) is stable above 23–25 GPa and the preferred orientation that develops during mantle convection could be expressed in seismic anisotropy. Thus deformation mechanisms of this mineral are of great importance and currently only with radial DAC experiments can we investigate the evolution of preferred orientation *in situ* at lower mantle pressure.

In recent DAC experiments perovskite has been produced from olivine (Mg_2SiO_4), ringwoodite (Mg_2SiO_4) and enstatite ($MgSiO_3$) as starting materials [25, 40]. If enstatite is used, the product is pure perovskite; with olivine and ringwoodite it is a mixture of perovskite and periclase (MgO). Figure 9 displays some portions of unrolled images, highlighting the strong diffraction lines 004 + 220, with the main intensity contribution from 004. In all experiments significant preferred orientation was produced, visible in the intensity variations.

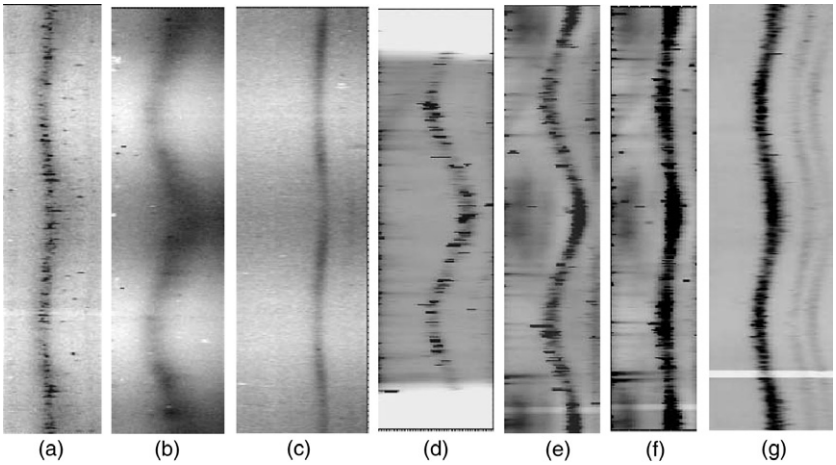

Figure 9. 004 + 220 diffraction lines of $MgSiO_3$ perovskite measured *in situ* for different experimental conditions. (a) Perovskite transformed from olivine at 25 GPa, (b) after increasing pressure to 43 GPa (APS-GSECARS). (c) Perovskite transformed from ringwoodite at 43 GPa (APS-GSECARS). (d) Perovskite transformed from enstatite at 50 GPa, (e) increase in texture strength after maintaining stress for 24 h, (f) change in pattern and microstructure after laser heating at 1400 °C for 30 min (APS-GSECARS). (g) Perovskite transformed from enstatite at 44 GPa (APS-HPCAT).

But even a qualitative glance reveals considerable differences, depending on starting material and conditions.

When perovskite transforms from olivine at 25 GPa first a spotty pattern develops due to a fairly large grain size produced during the phase transformation induced by laser heating at 1200 °C (figure 9(a)). Upon increasing pressure to 43 GPa, stresses become more pronounced and effective grain size is reduced by plastic deformation, resulting in a smooth intensity distribution with a regular pattern (figure 9(b)). When perovskite is formed from ringwoodite at 43 GPa a different but well defined texture is present with a maximum intensity of the 004 diffraction line between compression and extension direction (figure 9(c)). An interesting experiment is with enstatite as starting material. Unfortunately in this case a small (10 μm) beam had to be used and grain size was rather coarse after transformation at 1350 °C and 40 GPa, resulting in a spotty pattern and poor grain statistics. Increasing pressure to 50 GPa, texture is first moderate (figure 9(d)) but increases when the DAC is maintained at that pressure for 24 h (figure 9(e)), with a main maximum parallel to the compression direction and a subsidiary maximum perpendicular to it. This is analogous to a creep experiment where deformation occurs at constant stress. Upon heating at 1400 °C for thirty minutes stresses are reduced (less curvature) and the grain structure changes, documenting on-going recrystallization (figure 9(f)). Maxima parallel and perpendicular to the compression direction are of equal strength. A second experiment with enstatite as starting material, but a boron-epoxy gasket, produced a similar texture pattern at 44 GPa (figure 9(g)).

Figure 9 only displays the intensity distribution of two overlapped diffraction lines, illustrating qualitative differences. Some images could be quantitatively analysed with the Rietveld method, as illustrated in section 2, to obtain orientation distributions and inverse pole figures (figure 10). When perovskite transforms from olivine, there is shortly after the transformation a maximum in the inverse pole figure near (100) (figure 10(a)). With increasing pressure and deformation a second concentration develops near (011) (figure 10(b)).

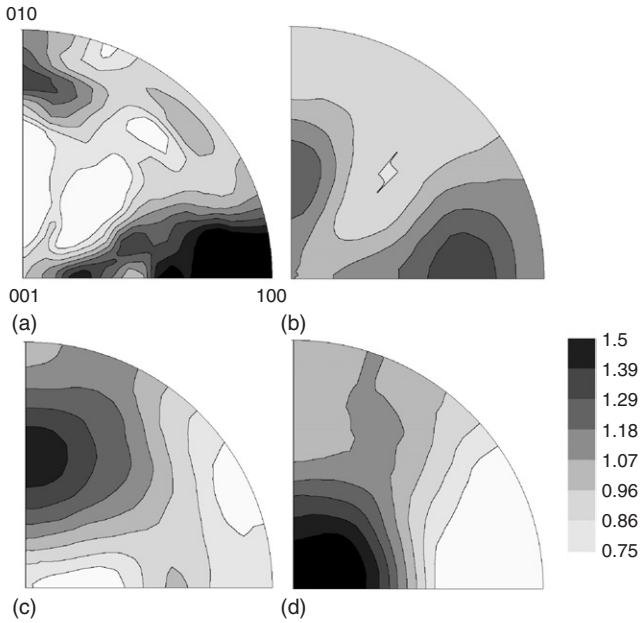

Figure 10. Inverse pole figures for orthorhombic $MgSiO_3$ perovskite. (a) Transformed from olivine at 25 GPa (APS-GSECARS) (compare figure 9(a)), (b) increasing pressure to 43 GPa (APS-GSECARS) (compare figure 9(b)), (c) transformed from ringwoodite at 43 GPa (APS-GSECARS) (compare figure 9(c)), (d) transformed from enstatite at 44 GPa (APS-HPCAT) (compare figure 9(g)). Equal area projection, linear contours.

Table 2. Slip systems assumed in polycrystal plasticity simulations of orthorhombic perovskite. Critical shear stress coefficients (CRSS) and average activity (in %) at 20% strain (see figure 11 for corresponding texture types).

Slip system	CRSS	Activity	CRSS	Activity	CRSS	Activity	CRSS	Activity
	A		B		C		D	
(100)[010]	1	40	5	18	5	0	5	8
(001)[100]	5	0	5	18	1	44	5	8
(001)[100]	5	41	1	47	1	44	5	0
(001)⟨110⟩	20	18	20	19	20	11	1	84

We tentatively attribute the (100) maximum to (110) twinning [41]. When perovskite forms from the intermediate phase ringwoodite, the main maximum is near (011) (figure 10(c)). Perovskite transforming from enstatite displays a maximum near (001), with a minimum at (100) (figure 10(d)). We think that the (011) and (001) texture types were produced by slip.

In order to estimate deformation mechanisms, we compare the experimental texture with polycrystal plasticity simulations, assuming slip systems that have been proposed: (010)[100], (001)[100], (100)[010] and (001)⟨110⟩ [42–44]. A single crystal diffraction study did not find evidence for ⟨110⟩ slip [45]. We report results for four models of slip systems with widely different critical shear stress coefficients (table 2). Surprisingly texture patterns are not dramatically different (figure 11). For dominant (100)[010] slip (model A, figure 11(a)), there is still significant (001)[100] slip to maintain compatibility, and a broad girdle between (001) and (100) is quite different from observed textures. The best match for the texture of perovskite

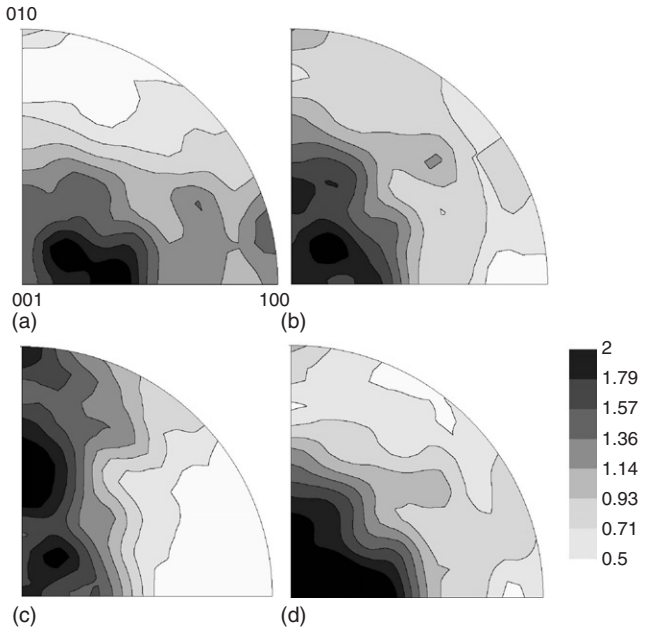

Figure 11. Polycrystal plasticity simulations for orthorhombic perovskite. For slip systems, critical resolved shear stress coefficients and activities see table 2. (a) Model A, (b) model B, (c) model C and (d) model D. Equal area projection, linear contours.

transformed from ringwoodite (figure 10(c)) is obtained if (010)[100] and (001)[100] slip are equally active (model C, figure 11(c)). The texture of perovskite transformed from enstatite (figure 10(d)) can be explained if (001)[100] is the dominant slip system (model B, figure 11(b)) or if the slip system is (001)⟨110⟩ (model D, figure 11(d)). At this point interpretations are tentative and more experiments are needed. Issues not considered in the simulations are complications introduced by multiple phases and mechanical twinning that may influence texture patterns [41]. From a comparison of texture strength in experiments and simulations we imply an overall strain of about 20%.

One conclusion of experiments and simulations is quite definite: all observed textures are strongly ”orthorhombic”, requiring slip systems also to be orthorhombic and not pseudo-cubic. In inverse pole figures pole densities at (100), (010) and (001) are very different. This indicates that cubic perovskites are poor analogues to infer the deformation behaviour in the lower mantle [46]. This is consistent with elastic properties and structural features that become more orthorhombic with increasing pressure and temperature [47, 48].

The $MgSiO_3$ perovskite emerges as a very complex and interesting system with large texture variations depending on experimental conditions. In addition to the range of results described above, some radial DAC experiments produced insignificant textures [40] and experiments on pseudo-cubic $CaSiO_3$ produced a texture compatible with {110} slip [49].

3.4. Iron

Pure iron is the first material where radial diffraction DAC measurements were used to extract quantitative texture information [50]. In this case, and in contrast to all other DAC experiments discussed in this paper, white x-rays were used and diffraction effects were recorded with an energy-dispersive point detector. Iron is of considerable importance in geophysics because it

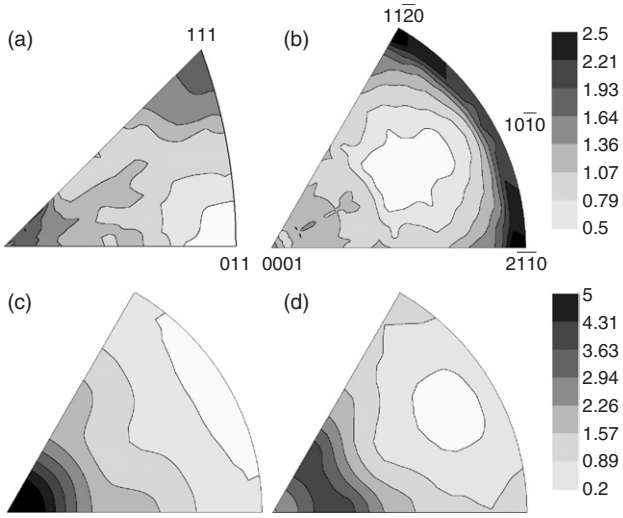

Figure 12. Radial DAC deformation of iron. (a) Bcc iron in a mixture with MgO deformed to a pressure of 12.4 GPa, (b) immediately after phase transformation to hcp at 17.7 GPa [53]. (c) Texture of hcp iron at 220 GPa [50]. (d) Polycrystal plasticity simulation favouring basal slip. Equal area projection, linear contours.

constitutes the solid inner core, where seismic anisotropy was documented that may be caused by texturing [51]. At ambient temperature iron transforms from a bcc structure to hcp at 15 GPa. Experiments at 220 GPa, close to pressures in the centre of the earth, reveal a strong (0001) texture (figure 12(c)), that can only be explained with significant basal slip (figure 12(d)). This slip system has been predicted for hcp iron, based on theory [52].

The investigation of iron was continued with monochromatic x-rays and CCD detectors, at lower pressures [53]. In a mixture of iron and MgO, bcc iron develops a texture with {111} lattice planes perpendicular to the compression direction (figure 12(a)). This is typical of bcc metals and attributed to dominant $\{110\}\langle\bar{1}11\rangle$ slip [54]. Above 15 GPa the transition to hcp occurs and the transformation texture has a main concentration at $\{11\bar{2}0\}$ (figure 12(b)), which is qualitatively consistent with the Burgers' relationship [55] that predicts close-packed bcc directions {111} to become aligned with close-packed hcp directions $\{11\bar{2}0\}$, though this is accompanied by variant selection, most likely influenced by stress. Upon further increase in pressure and stress, the hcp $\{11\bar{2}0\}$ transformation texture changes to a (0001) deformation texture (figure 12(c)).

4. Discussion

Recent radial diffraction geometry DAC experiments have illustrated that oxides and silicates become ductile at pressures above 5 GPa even at room temperature, activating slip systems and producing deformation textures. Quantitative texture analysis requires determination of the orientation distribution, which is now feasible from radial DAC diffraction images. This is much more informative than a merely qualitative assessment of relative intensity differences that are difficult to interpret, especially if polychromatic radiation is used. Only quantitative texture patterns can be interpreted with some degree of confidence.

In cases where textures can be compared with conventional deformation experiments at similar conditions, and with polycrystal plasticity simulations based on known slip systems, the patterns are consistent as illustrated for olivine and periclase. With polycrystal plasticity

we can further estimate an overall strain of about 10–20% for DAC deformation experiments conducted so far. Image analysis without imposing sample symmetry establishes that strain is approximately axially symmetric, confirming results from finite element simulations [7], except for experiments with obvious deficiencies and highly ductile materials such as fcc metals [56].

If active deformation mechanisms are not known they can be implied from texture patterns by comparisons with polycrystal plasticity simulations, as we have shown here for magnesiowuestite and perovskite. In some cases these room temperature slip systems agree with slip systems predicted based on theory, as in the case of post-perovskite ([57] versus 6) and ringwoodite ([58] versus 4). In MgO different slip systems are active at high temperature [17, 27–29]. In the future it may be possible to extrapolate slip system activity to different pressure and temperature conditions and the combined information contributes to a better understanding of deformation in the deep earth.

Naturally the DAC deformation technology needs to be refined in the future. Foremost it is necessary to be able to control pressure changes and associated stress increase *in situ*, which could not be done in the current experiments, though such methods are used in axial geometry DAC experiments [59]. It would be highly desirable to investigate slip systems at higher temperature. Also here methods exist for *in situ* heating by resistance furnaces [60–62] as well as laser heating [63] but require non-trivial modifications for radial diffraction that are currently not available at high pressure beamlines. With *in situ* control of pressure and temperature it will become possible to investigate texture changes during initial deformation and particularly address issues of texture memory during phase transformations that may indicate martensitic mechanisms, which have been proposed for the olivine–ringwoodite transition but could not be verified in these experiments [64, 65].

With microbeam techniques it may become possible to investigate microstructure and orientation grain by grain [66]. A further limitation of the current radial DAC technology is the relatively limited strain in compressive geometry. Low strain is preferable for identification of intracrystalline slip systems from textures since polycrystal plasticity theories break down at large strains, with significant strain hardening [67], activation of subordinate systems and grain boundary sliding to provide compatibility as well as dynamic recrystallization [68]. Rotational DAC cells that produce torsion deformation have been developed and provide exciting opportunities for large strain experiments [69, 70]. Many of these experimental improvements of DAC technology are currently under development and should become available for users in the near future.

There is a wide range of applications of DAC deformation experiments to new materials to not only explore deformation mechanisms at ultrahigh pressure but also to better understand processes such as texture changes and variant selection during phase transformations, or changes that occur during static and dynamic recrystallization. Obviously DAC experiments only provide limited information to infer rheological conditions in the deep earth. Whereas they may never yield reliable stress–strain curves, we have illustrated that they provide information on texture development that is a fairly robust indicator of intracrystalline mechanisms, responsible for grain rotations to achieve anisotropic polycrystal properties. This information can be used to interpret observed seismic anisotropy patterns in the deep earth [71].

Acknowledgments

The authors are grateful for access to high pressure beamlines at the Advanced Light Source (LBNL 12.2.2), the Advanced Photon Source (ANL) GSECARS and HPCAT where experiments were performed, and help from beamline scientists. We are indebted to Haozhe

Liu and COMPRES for a stimulating workshop at APS that generated a lot of interest in DAC deformation experiments. HRW is appreciative of Dave Mao for seducing him into this fascinating field of research. The work has been supported by CDAC, NSF and IGPP-LANL. S Merkel and S Speziale acknowledge support from the Miller Institute of Basic Research at Berkeley and C E Tommaseo from the Deutsche Forschungsgemeinschaft.

References

[1] Manghnani M H and Syono Y (ed) 1987 *High-Pressure Research in Mineral Physics. Geophysical Monograph* vol 39 (Washington, DC: Amer. Geophys. Union)
[2] Wang Y, Durham W B, Getting I C and Weidner D J 2003 *Rev. Sci. Instrum.* **74** 3002–11
[3] Yamazaki D and Karato S I 2001 *Rev. Sci. Instrum.* **72** 4207–11
[4] Carrez P, Cordier P, Mainprice D and Tommasi A 2006 *Eur. J. Mineral.* at press
[5] Miranda C R and Scandolo S 2005 *Comput. Phys. Commun.* **169** 24–7
[6] Oganov A R, Martonák R, Laio A, Raiteri P and Parrinello M 2005 *Nature* **438** 1142–4
[7] Merkel S, Hemley R, Mao H-K and Teter D M 2000 Science and technology of high pressure *Proc. AIRAPT* vol 17, ed M H Manghnani, W J Nellis and M F Nicol, pp 68–73
[8] Kinsland G L and Bassett W A 1976 *Rev. Sci. Instrum.* **47** 130–2
[9] Hemley R J, Mao H-K, Shen G, Badro J, Gillet P, Hanfland M and Häusermann D 1997 *Science* **276** 1242–5
[10] Singh A K, Mao H-K, Shu J and Hemley R J 1998 *Phys. Rev. Lett.* **80** 2157–60
[11] Frost H J and Ashby M F 1982 *Deformation Mechanism Maps* (Toronto: Pergamon) p 166
[12] Yamazaki D and Karato S 2001 *Am. Mineral.* **86** 385–91
[13] Griggs D T 1967 *Geophys. J. R. Astron. Soc.* **14** 19–31
[14] Jung H and Karato S-I 2001 *Science* **293** 1460–2
[15] Karato S I, Paterson M S and Fitzgerald J D 1986 *J. Geophys. Res.* **91** 8151–76
[16] Katayama I, Jung H and Karato S I 2004 *Geology* **32** 1045–8
[17] Merkel S, Wenk H-R, Shu J, Shen G, Gillet P, Mao H-K and Hemley R J 2002 *J. Geophys. Res.* **107 2271** (doi:10.1029/2001JB000920)
[18] Mao H K, Shu J, Fei Y and Hemley R J 1996 *Phys. Earth Planet. Inter.* **96** 135–45
[19] Merkel S and Yagi T 2005 *Rev. Sci. Instrum.* **76** 046109 (doi:10.1063/1.1884195)
[20] Lonardelli I, Wenk H-R, Goodwin M and Lutterotti L 2005 *J. Synchrotron Res.* **12** 354–60
[21] Lutterotti L, Matthies S and Wenk H-R 1999 *Int. U. Crystallogr. Comm. Powder Diffraction Newslett.* **21** 14–5
[22] Ischia G, Wenk H-R, Lutterotti L and Berberich F 2005 *J. Appl. Crystallogr.* **38** 377–80
[23] Montagner J P and Tanimoto T 1990 *J. Geophys. Res.* **95** 4797–819
[24] Carter N L and Ave'Lallemant H G 1970 *Geol. Soc. Am. Bull.* **81** 2181–208
[25] Wenk H-R, Lonardelli I, Pehl J, Devine J, Prakapenka V, Shen G and Mao H-K 2004 *Earth Planet. Sci. Lett.* **226** 507–19
[26] Raleigh C B 1968 *J. Geophys. Res.* **73** 5391–406
[27] Heidelbach F, Stretton I, Langenhorst F and Mackwell S 2003 *J. Geophys. Res.* **108** 2154 (doi:10.1029/2001JB001632)
[28] Stretton I, Heidelbach F, Mackwell S and Langenhorst F 2001 *Earth Planet. Sci. Lett.* **194** 229–40
[29] Yamazaki D and Karato S I 2002 *Phys. Earth Planet. Inter.* **131** 251–67
[30] Carter N L and Heard H C 1970 *Am. J. Sci.* **269** 193–249
[31] Tommaseo C E, Merkel S, Speziale S, Devine J and Wenk H-R 2006 *Phys. Chem. Mineral.* **33** 84–97
[32] Bonczar L J and Graham E K 1982 *J. Geophys. Res.* **87** 1061–78
[33] Jacobsen S D, Reichmann H-J, Spetzler H A, Mackwell S J, Smyth J R, Angel R J and McCammon C A 2002 *J. Geophys. Res.* **107** 2037 (doi:10.1029/2001JB000490)
[34] Jacobsen S D, Lin J-F, Angel R J, Shen G, Prakapenka V B, Dera P, Mao H-K and Hemley R J 2005 *J. Sychrotron Radiat.* **12** 577–83
[35] Mao W, Shu J, Hemley R J and Mao H-K 2002 *J. Phys. Condens. Matter* **14** 11349–54
[36] Shu J, Mao H-K, Hu J, Fey Y and Hemley R J 1998 *Neues Jahrb. Mineral. Abh.* **172** 309–23
[37] Ito E M and Takahashi E 1989 *J. Geophys. Res.* **94** 10637–46
[38] Lines M E and Glass A M 1977 *Principles and Applications of Ferroelectrics and Related Materials* (Oxford: Clarendon)
[39] Galasso S 1969 *Structure, Properties and Preparation of Perovskite Type Compounds* (New York: Pergamon) p 207

[40] Merkel S, Wenk H-R, Badro J, Montagnac J, Gillet P, Mao H-K and Hemley R J 2003 *Earth Planet. Sci. Lett.* **209** 351–60
[41] Wang Y, Guyot F, Yeganeh-Haeri A and Liebermann R C 1990 *Science* **248** 468–71
[42] Besson P, Poirier J P and Price G D 1996 *Phys. Chem. Minerals* **23** 337–44
[43] Poirier J P, Beauchesne S and Guyot F 1991 *Perovskites, A.G.U. Monograph* vol 45, ed A Navrotsky and D Weidner (Washington, DC: Amer. Geophys. Union) pp 119–23
[44] Wright K, Price G D and Poirier J P 1992 *Phys. Earth Planet. Inter.* **74** 9–22
[45] Cordier P, Ungár T, Zsoldos L and Tichy G 2004 *Nature* **428** 837–40
[46] Karato S-I, Zhang S and Wenk H-R 1995 *Science* **270** 458–61
[47] Oganov A R, Brodholt J P and Price G D 2001 *Nature* **411** 934–7
[48] Wentzcovitch R M, Karki B B, Cococcioni M and de Gironcoli S 2004 *Phys. Rev. Lett.* **92** 018501 (doi:10.1103)
[49] Miyagi L, Merkel S, Yagi T, Sata N, Ohishi Y and Wenk H-R 2006 *J. Phys. Condens. Matter* **18** S995–1005
[50] Wenk H-R, Matthies S, Hemley R J, Mao H-K and Shu J 2000 *Nature* **405** 1044–7
[51] Song X 1997 *Rev. Geophys.* **35** 297–313
[52] Poirier J P and Price G D 1999 *Phys. Earth Planet. Inter.* **110** 147–56
[53] Merkel S, Wenk H-R, Gillet P, Mao H-K and Hemley R J 2004 *Phys. Earth Planet. Inter.* **145** 239–51
[54] Rollett A D and Wright S I 2000 *Texture and Anisotropy. Preferred Orientations in Polycrystals and Their Effect on Materials Properties* 2nd Paperback edn, ed U F Kocks, C N Tomé and H-R Wenk (Cambridge: Cambridge University Press) chapter 5, pp 178–238
[55] Burgers W G 1934 *Physica* **1** 561–86
[56] Speziale S, Lonardelli I, Miyagi L, Pehl J, Tommaseo C E and Wenk H-R 2006 *J. Phys. Condens. Matter* **18** S1007–20
[57] Merkel M, Kubo A, Miyagi L, Speziale S, Duffy T S, Mao H-K and Wenk H-R 2006 *Science* **311** 644–6
[58] Wenk H-R, Ischia G, Nishiyama N, Wang Y and Uchida T 2005 *Phys. Earth Planet. Inter.* **152** 191–9
[59] Liu J, Li X D and Li Y C 2002 *J. Phys. Condens. Matter* **14** 10505–9
[60] Dubrovinskaia N and Dubrovinsky L S 2003 *Rev. Sci. Instrum.* **74** 3433–7
[61] Dubrovinsky L S, Saxena S K and Lazor P 1997 *Geophys. Res. Lett.* **24** 1835–8
[62] Dubrovinsky L S, Dubrovinskaia N, Annesten H, Hålenius H and Harryson H 2001 *Eur. J. Mineral.* **13** 857–61
[63] Ming L C and Bassett W A 1974 *Rev. Sci. Instrum.* **45** 1115–8
[64] Burnley P C and Green H W 1989 *Nature* **338** 753–6
[65] Poirier J P 1981 *Phys. Earth Planet. Inter.* **26** 179–87
[66] Larson B C, Yang W, Ice G E, Budal J D and Tischler J Z 2002 *Nature* **415** 887–90
[67] Kocks U F and Mecking H 2003 *Prog. Mater. Sci.* **48** 171–273
[68] Gottstein G 2002 *Proc. ICOTOM 13; Mater. Sci. Forum* **408–412** 1–24
[69] Novikov N V, Polotnyak S B, Shvedov L K and Levitas V I 1999 *J. Superhard Mater.* **21** 36–48
[70] Levitas V I 2004 *Phys. Rev.* B **70** 184118
[71] Wenk H-R, Speziale S, McNamara A K and Garnero E J 2006 *Earth Planet. Sci. Lett.* **245** 302–14